Geotechnical Testing Journal

doi:10.1520/GTJ20240152 / Vol. 48 / No. 4 / 2025 / available online at go.astm.org/pubs

David Hercules Marx[1] and Jorge Gabriel Zornberg[2]

Experimental Setup to Measure the Development of Shear Bands in Transparent Sand

Reference

D. H. Marx and J. G. Zornberg, "Experimental Setup to Measure the Development of Shear Bands in Transparent Sand," *Geotechnical Testing Journal* 48, no. 4 (July/August 2025): 509–532. https://doi.org/10.1520/GTJ20240152

ABSTRACT

A triaxial setup was developed to quantify the development of shear bands in transparent specimens. Transparent sand was prepared by index-matching fused quartz with a mixture of mineral oils. Latex membranes were found to be incompatible with the oil used in the transparent soil technique. Consequently, a custom, transparent, silicone triaxial membrane was developed for the triaxial testing. Water-saturated fused quartz tested with the custom membranes had an equivalent stress-strain response to those tested with latex membranes. Dense triaxial specimens prepared from a uniformly graded fused quartz, saturated with mineral oil, were tested at three different confining stresses. The displacement on two laser-illuminated sections through the specimens was measured using digital image correlation. From these displacement fields strain fields were developed that were used to orient the shear bands in 3-D. Subsequently, the inclination, orientation, and width of the shear bands were calculated. Consistent with the bulging mode of failure observed, a family of conjugate shear bands, rather than a discrete slip, was measured in each specimen. The shear bands were between $8.6 \cdot D_{50} - 11.5 \cdot D_{50}$ wide for the particle size and range of confining stresses evaluated in this study. Finally, the shear band inclination was found to increase with an increase in confining stress.

Keywords

triaxial testing, transparent sand, shear band, digital image correlation

Manuscript received July 25, 2024; accepted for publication April 3, 2025; published online June 13, 2025. Issue published July 1, 2025.

[1] Maseeh Department of Civil, Architectural, and Environmental Engineering, University of Texas at Austin, 301 E. Dean Keeton St., Austin, TX 78712, USA (Corresponding author), e-mail: dawie.marx@utexas.edu, https://orcid.org/0000-0002-5610-5755

[2] Maseeh Department of Civil, Architectural, and Environmental Engineering, University of Texas at Austin, 301 E. Dean Keeton St., Austin, TX 78712, USA, https://orcid.org/0000-0002-6307-1047

Introduction

The study of shear band development in soils is intertwined with the development of triaxial testing. A shear band is a region in the soil body that strains significantly more

than the surrounding, comparatively rigid, body of soil (Scrapelli and Wood 1982). Multiple techniques have been developed to measure shear band propagation under triaxial loading. However, no technique is perfect. For example, x-ray imaging of specimens embedded with lead shot allowed for the internal deformation of the specimen to be measured at full scale but at the cost of spatial resolution (Nemat-Nasser and Okada 2001; Otani, Mukunoki, and Obara 2000; Roscoe 1970; Scrapelli and Wood 1982). Alternatively, surface measurements of shear bands were made at high spatial and temporal resolution (Leib, Sharma, and Penumadu 2021; Li et al. 2016; Rattez et al. 2022). However, surface projections of shear bands do not necessarily represent the internal deformation of the specimen. Internal deformation can be measured at high spatial resolution in specialized CT scanning setups (Cheng and Wang 2018; Desrues and Viggiani 2004). However, the attenuation of x-rays by soil minerals limits the size of these specimens. In addition, the x-ray images need to be taken at discrete intervals because of the slow imaging process.

In this study, an alternative shear band measurement technique involving the use of a soil surrogate, known as transparent sand, is presented. The technique allows for the measurement of shear bands from internal deformations, at both high temporal and spatial resolution.

Overview of Transparent Sand

Transparent soils are a family of soil surrogates that can be used to study the internal deformation of a soil body under load. Some of the surrogates, such as amorphous silica and Laponite® RD, mimic the behavior of fine-grained materials (i.e., clays and silts). Others, such as silica beads and fused quartz, can be used to model the behavior of granular materials (i.e., sands and gravels; Iskander, Bathurst, and Omidvar 2015). Fused quartz is transparent, nearly pure silica in amorphous form. In this study, fused quartz saturated with mineral oil was used as a transparent sand surrogate.

OPTICAL BEHAVIOR OF TRANSPARENT SAND

When a ray of light strikes a fused quartz particle, the surface of the particle both reflects and transmits the light. The portion of light reflected is proportional to the difference in the refractive index of the propagating medium (e.g., air) and that of the object (Hecht 2016). The greater the difference in refractive indexes, the more light is reflected. If all the light is reflected, the object appears opaque. Light traveling toward a pile of fused quartz particles will be reflected in all directions. Consequently, the particles will appear opaque as shown in the top left quarter of **figure 1**.

When fused quartz is saturated with a liquid with a matching refractive index, light transmits through the mixture, rather than reflecting. Thus, the sand appears transparent. An example of fused quartz saturated with mineral oil is shown in the lower left portion of **figure 1**. However, it is not feasible to perfectly match the refractive indexes of the quartz and the oil. This inevitable, minor mismatch results in particle edges being faintly visible. When concentrated light, such as a laser, is shined into the specimen, it will refract away from the laser plane at the particle edges, illuminating the particles on that plane (Peng and Zornberg 2019). The right half of **figure 1** illustrates the use of a laser to illuminate a section through a body of transparent sand. By tracking the displacement of the particles on such sections, the development of shear bands can be studied.

Any impurities in the oil, such as specks of dust or air bubbles present, will lead to the diffuse refraction of light transmitting through the transparent sand. If too many of these impurities are present, the transparent sand will appear opaque. Furthermore, light from the sheet laser will be refracted by both these impurities and the particle edges, obfuscating the particle edges and resulting in a fuzzy image.

MECHANICAL BEHAVIOR OF TRANSPARENT SAND

The use of oil as the saturating liquid, rather than water, has implications on the mechanical response of the fused quartz. Under shear loading, the peak strength of the oil-saturated fused quartz has been reported to be lower than

FIG. 1

Typical examples of partially saturated transparent sand (left) and a saturated, laser-illuminated section of transparent sand (right).

the water-saturated equivalent (Carvalho et al. 2015; Derksen, Ziegler, and Fuentes 2021; Ezzein and Bathurst 2011). However, the strength at large strain is typically independent of the saturation fluid.

In addition to the slightly lower strength, so-called "slip-stick" behavior often occurs during shear (e.g. Carvalho et al. 2015; Derksen, Ziegler, and Fuentes 2021; Ezzein and Bathurst 2011). Slip-stick behavior is characterized by cycles of brittle drops in deviatoric stress, followed by an increase to the previous stress level. These drops are due to load bearing chains buckling and reforming (Ezzein and Bathurst 2011; Ozbay and Cabalar 2016; Tordesillas and Muthuswamy 2009). The low interparticle surface friction of fused quartz, combined with the lubricating effect of oil, results in a comparatively pronounced slip-stick behavior (Galaz, Espíndola, and Melo 2018).

In addition to the shear behavior, the hydraulic conductivity of the sand is affected by using oil as a saturating medium. Because of the comparatively high viscosity of oil, the hydraulic conductivity can be one to two orders of magnitude lower than that of water-saturated specimens (Carvalho et al. 2015; Ezzein and Bathurst 2011). Finally, Ezzein and Bathurst (2011) found that, under one-dimensional compression, oil- and water-saturated specimens behaved similarly.

Experimental Setup

An automated triaxial setup with a custom, transparent silicone membrane and an imaging frame was developed to measure the shear bands that developed in transparent sand. The shear bands were quantified based on the displacements measured on two laser-illuminated sections through the triaxial specimens.

TRIAXIAL TESTING SETUP

The automated triaxial testing setup used for the study was manufactured by Trautwein GeoTac. The system consisted of a load actuator and two volume pumps: one to control the cell pressure and another to control the back pressure applied. Each of the volume pumps were connected to a bladder accumulator. These accumulators separated the water in the pumps from the oil used to apply the back pressure and cell pressure.

The cell pressure was measured at the base of the cell. The pore fluid pressure was measured at a bridged connection between the drainage lines from the top and bottom caps. Both pressure transducers had a capacity of 790 kPa. Depending on the expected loads either a 2.2 kN or an 8.9 kN load cell was used to measure the deviatoric stress applied.

Some of the specimens were tested using lubricated platens for equivalency with stabilized specimens prepared for a companion study (Marx, Kumar, and Zornberg 2023). The lubricated platens each consisted of two layers of soaked silicone disks lubricated with vacuum grease, stacked on top of a polished, enlarged aluminum platen. Black silicone rubber was used for the disks to limit stray reflection of the lasers. In the center of each of the lubricated platens, a short drainage pipe stopped with filter paper was placed. In addition to providing drainage, the pipes also anchored the specimen against lateral sliding (Vernese and Lee 1977).

Similar to Olson and Lai (2004), grease squeezed out of the lubricated platens into the specimen for some of the tests. This may have been due to the viscosity of the vacuum grease increasing as it dissolved in the mineral oils. However, the volume of sand affected was less than 10 mm in diameter, and thus the effect on the measured behavior of the fused quartz was considered negligible.

A backstop of optical-grade flock paper was placed inside the cell to limit the reflection of the laser. All other reflective surfaces were also covered by flock paper.

IMAGING FRAME

The imaging frame shown in **figure 2** was used to capture images of the laser-illuminated sections through the specimens. The frame consisted of lasers, cameras, and frames with image alignment markers (light-emitting diode [LED] lights). The frames for the image alignment markers were fixed on a plane parallel to that of the lasers.

A single laser-camera pair can measure displacement across one section through a specimen. Shear bands are planar structures that may develop along any orientation in the specimen. Thus, displacement was measured across two sections through the specimen, intersecting at 60° to each other, to better capture the development of the shear bands.

A 450-mW red sheet laser (COMPACT-450G-638) and a 350-mW red sheet laser (COMPACT-350G-638), both with a wavelength of 638 nm, were used to illuminate the two sections through the specimens. The lasers were manufactured by World Star Tech. Each of the laser-illuminated sections was imaged with a Canon EOS 5DS R camera fitted with a Sigma 50 mm f/1.4 lens. These cameras had 36 mm × 24 mm (full-frame) sensors with 50.6 usable megapixels. Each pixel is 4.14 μm by 4.14 μm square.

FIG. 2 Imaging frame used to measure shear band development (from Marx, Kumar, and Zornberg 2023).

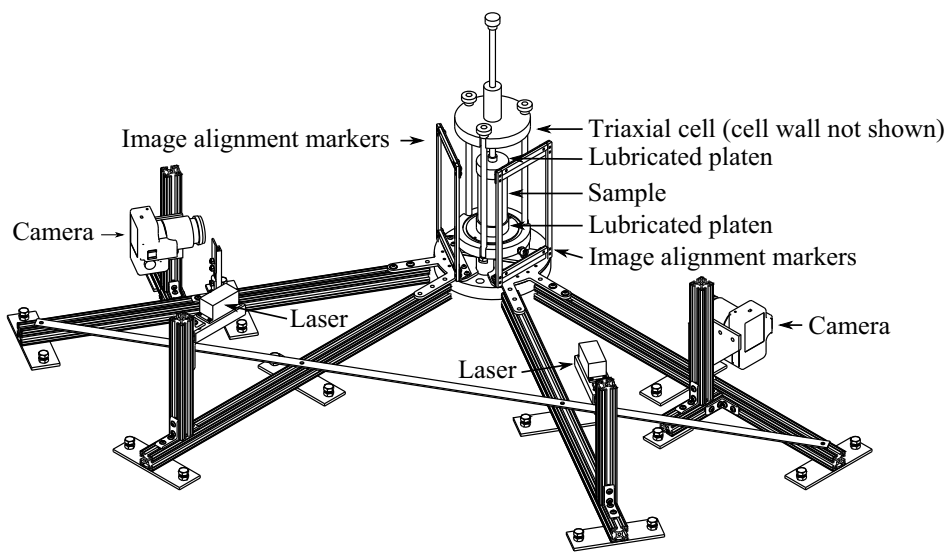

A mirror was placed against the back of the frames supporting the image alignment markers (i.e., parallel to the laser planes) to assist with aligning the cameras perpendicular to the laser planes. The position of each camera was adjusted until the reflection of the lens in the mirror was centered in the camera's viewfinder.

The images captured by the cameras had to be synchronized to the sensor readings in order to correlate the observed shear band to the stress state in the specimen. An Arduino Uno microcontroller was used for this synchronization. The microcontroller was connected to a host computer over a serial connection. First, a Python script running on the computer turned one of the lasers on over another serial connection. Next, the Python script instructed the microcontroller to trigger the camera perpendicular to that laser. The microcontroller then closed the circuit of the camera's remote trigger (N3) socket. An optocoupler was placed between the camera and the microcontroller to protect the camera against potential electrical surges. Simultaneously, the microcontroller also output an analog voltage pulse through a connected MCP4725 digital-to-analog (DAC) converter. This analog pulse from the DAC was recorded by the triaxial's data acquisition system together with the other sensor readings. The magnitude of the pulse differed depending on which camera-laser pair was triggered. Thus, the images could be synchronized to the sensor readings. Images were captured at a rate of approximately 0.02 % axial strain.

Image Alignment Frame

Minute movement of the cameras may occur during a test because of the operation of the mechanical shutters of the cameras. These movements are random in nature and insignificant when comparing two images. However, over a series of 700 images, the cumulative movement may become significant when measurements of small strains are of concern. Thus, markers were used to align the images, as is typically done in centrifuge testing (White, Take, and Bolton 2003).

Red LED lights were used as markers. The LEDs surrounded the specimen and were fastened to two alignment frames following the work of Stanier, Black, and Hird (2012). During postprocessing of the images, the images were translated and rotated until the LED markers overlapped. The intensity of the LEDs were optimized to be bright enough for the centers to be accurately calculated but not so bright that the light interferes with the refraction from the particle edges (Stanier 2011).

Laser Positioning

The laser beams follow a Gaussian distribution–shaped profile. That is, on a section perpendicular to the beam, the intensity is at a maximum at the beam axis and decreases toward the edges. For lower quality lasers the decline is gradual, resulting in a less focused beam. The width of the laser beam also varies along the length of propagation because of beam divergence. The location where the beam width is a minimum is known as the beam waist (Hecht 2016).

The edges of all particles intersected by the laser will refract the light away from the direction the laser is propagating. This illuminates the particle outlines. When the width of the beam is greater than the diameter of a fused quartz particle, more than one particle will be illuminated at a given distance and height along the laser plane. Thus, the outlines of the particles will overlap in the images. Consequently, displacement will be measured along multiple consecutive planes in the specimen. Thus, it is critical to ensure that the beam waist is smaller than the particle diameters and that the specimen is placed at the location of the beam waist.

The lasers used in this study were reported to have a divergence angle of <1 mrad. The beam width was measured to vary from 5 mm at the extremes to 1 mm at the waist. For the COMPACT-450G-638 laser, the beam waist was at 750 mm from the aperture, and for the COMPACT-350G-638 laser, it was 600 mm from the aperture.

TRANSPARENT MEMBRANES

The latex membranes typically used for triaxial testing are opaque. Furthermore, latex tends to expand and becomes brittle when submerged in the mineral oils used in this study. This response can often be observed at the edges of a latex membrane after it has been in contact with the petroleum jelly used on the platens of a triaxial setup. Silicone rubber was identified as an alternative material with higher chemical resistance and inherent transparency.

Manufacturing

Custom, transparent membranes were constructed from 0.5 mm thick, medium-soft (40A durometer hardness), silicone sheets. Silicone rubber is not completely inert to the presence of mineral oils. Thus, the silicone was first soaked in mineral oil. The expansion of the silicone in the rubber plateaued at 11 % elongation after 48 hours, compared to the 50 % elongation observed for latex rubber. In addition, the silicone remained ductile after soaking for the deformation expected during a triaxial test. After 48 hours of soaking, the silicone was removed from the oil, wiped dry, and cut into a rectangle. The post-soak thickness of the membranes was approximately 0.8 mm. The rectangle was folded into a cylinder, and the edges were glued together with Sil-Poxy™ silicone rubber adhesive. An example of a transparent membrane installed on a triaxial pedestal is shown in figure 3.

Stiffness of the Silicone Membranes

In Table 1, the median, secant tensile stiffness of the silicone membranes is compared to that of the 0.7-mm thick latex membranes reported by La Rochelle et al. (1988). The stiffness of the membranes was measured following the method described by Henkel and Gilbert (1952). Results for commercial 0.7-mm thick membranes tested in this study are also shown. La Rochelle et al. (1988) noted that a membrane will experience a maximum of 20 % strain during a routine triaxial test. Consequently, they recommend using the membrane stiffness at 1 % axial strain for the beginning of the test and at 10 % axial strain for the remainder of the test. The silicone membranes were tested both after 48 hours of soaking and after being immersed in oil for a full triaxial testing cycle (saturation, consolidation, and shear).

The stiffness of the silicone membranes was comparable to that of latex membranes. The stiffness of both the silicone and the latex membranes decreased nonlinearly with axial strain. At higher levels of axial strain, the silicone membranes were slightly stiffer than the latex. Lastly, the continued exposure of the silicone membranes to oil during the testing procedure was found to further soften the membranes. However, this decrease in stiffness was negligible because of the minimal magnitude of the membrane corrections applied.

FIG. 3

A transparent membrane installed on the pedestal of a triaxial cell.

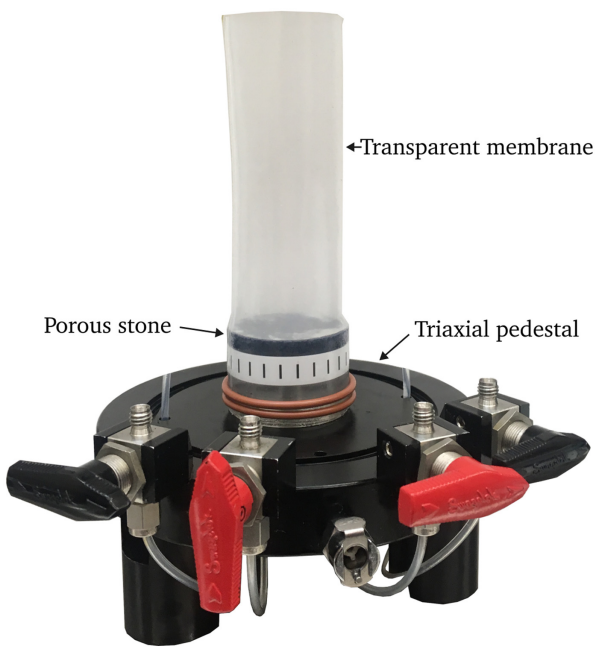

TABLE 1
Median tensile stiffness of the latex and silicone membranes

	Tensile Stiffness, [kPa]		
Material	1 %	10 %	20 %
Latex (La Rochelle et al. 1988)	1,440		1,025
Latex (this study)	1,522	872	836
Soaked silicone	1,418	994	978
Soaked silicone, tested	1,301	798	770

MATERIALS

Both oil- and water-saturated fused quartz were tested in this study. Whenever oil-saturation was used, the composite is referred to as "transparent sand." The fused quartz tested in this study was supplied by Xinyi Wanhe Mining Co., Ltd. Two different fused quartz sands were used in this study. The first sand (SU1) was used to confirm that the custom silicone membranes were equivalent to traditional latex membranes. The second sand (SU2) was used to study the difference between oil and water saturation on the mechanical behavior of fused quartz. In addition, SU2 was used to manufacture transparent sand to study shear band development.

SU1 was uniformly graded and ranged between 0.43 to 0.85 mm (40 to #20 sieve) in size (i.e., $D_{50} = 0.6$ mm). Following ASTM D4254-16, *Standard Test Methods for Minimum Index Density and Unit Weight of Soils and Calculation of Relative Density*, and ASTM D4253-16, *Standard Test Methods for Maximum Index Density and Unit Weight of Soils Using a Vibratory Table*, the minimum and maximum void ratio of SU1 was measured to be 0.73 and 1.01, respectively. The grading distribution of SU1 is shown in **figure 4**. SU1 was only saturated with water.

The second sand (SU2) was also uniformly graded and consisted of the material retained between the #8 (2.36 mm) and #6 (3.36 mm) sieves (i.e., $D_{50} = 2.9$ mm). The minimum and maximum void ratio of the sand was measured to be 0.72 and 0.85, respectively. Marx, Kumar, and Zornberg (2023) measured the median particle roundness of SU2 as 0.420 and the median area sphericity as 0.560 following Zheng and Hryciw (2015). The grading distribution of SU2 is shown in **figure 4**. Sand SU2 was saturated with both water and mineral oil. A mineral oil mixture of 52 % Puretol 7 and 48 % Paraflex HT 4 (Peng and Zornberg 2019), both manufactured by Petro-Canada, was used in this study.

FIG. 4
Particle size distributions of the fused quartz tested.

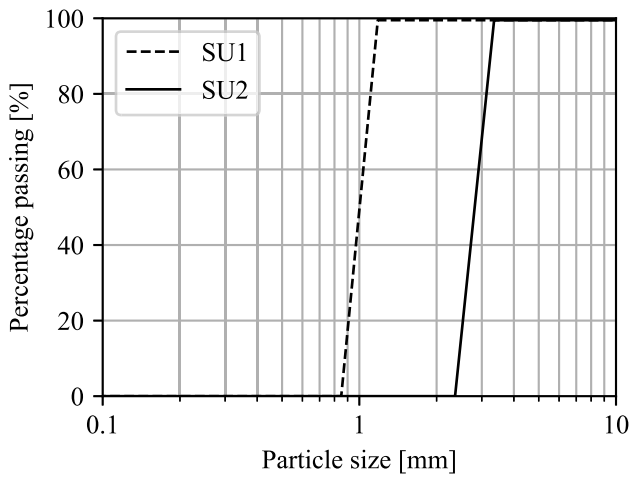

Experimental Methodology

SAMPLE PREPARATION, TESTING, AND ANALYSIS

Fifty-millimeter diameter triaxial specimens, 100 mm tall, were compacted in eight layers of 12.5 mm each. A custom compaction frame was fabricated in order to compact the specimen on top of the triaxial pedestal. Once compacted, the top platen was installed onto the specimen, clamped to the compaction mold, and then the specimen was saturated under vacuum. The vacuum pressure was kept below the final consolidation stress of the specimen. After this preliminary saturation, the compaction mold was removed. Leaks in the membrane could be visually identified from the air bubbles that were sucked into the specimen by the slight vacuum applied. These leaks were subsequently sealed with silicone rubber adhesive. The sample dimensions were measured after all leaks were sealed.

Next, the cell wall and top were installed, and the cell was placed in the load frame. Thereupon, the back pressure was gradually increased to 300 kPa while maintaining an effective stress of 13.8 kPa. The specimens were left overnight at the elevated back pressure to allow for the remaining air bubbles to dissolve. Any stray air bubbles would refract the laser, reducing the clarity of the images. After back pressure saturation, the B-value was measured, and the specimens were visually inspected for the presence of air bubbles. All specimens presented in this study had a B-value of $\geq$0.99.

Consolidation was typically completed within 10 minutes or less, as expected for a clean sand. After consolidation, the specimens were sheared at a rate of 6 % axial strain per hour. A slow rate of shear was required because of the relatively high viscosity of the oil and the restricted dissipation of pore pressure through the drainage pipes. In addition, the specimens had to be sheared slow enough that the particle movement would not result in a blurred image.

Standard area corrections (Head 2014) and membrane corrections (Duncan and Seed 1967) were applied to the measurements. The membrane stiffness at 10 % axial strain was used for the analysis. However, the membrane corrections were minimal (less than 5 % of the applied stress) because of the high strength of the quartz relative to the stiffness of both types of membranes.

TESTING PROGRAM

The scope of the testing program for this study, as summarized in Table 2, was three-fold: (1) evaluate the equivalency of the silicone membranes to conventional latex membranes, (2) compare the behavior of water- and oil-saturated fused quartz, and (3) quantify the development of shear bands in transparent sand.

First, triaxial testing was done on SU1 saturated with water using both latex and silicone membranes (SU1-L-W and SU1-S-W). SU1 was selected for the comparative study as the behavior of specimens constructed of a finer sand was judged to be less sensitive to relative particle arrangement, resulting in more consistent results. Correspondingly, the specimens were prepared dense to minimize variability. Thus, any difference in the measured behavior of the sand would be because of the material used for the membrane. The average postconsolidation relative density of these specimens was 85 %.

Second, the effect of using oil as a saturating liquid in place of water was investigated using sand SU2 (test series SU2-S-W and SU2-S-O-L). The specimens were prepared close to the maximum dry density of the sand.

TABLE 2
Summary of test results presented

Series Name	Sand	Void Ratio	Membrane Material	Saturating Fluid	Confining Stresses, kPa	Platens
SU1-L-W	SU1	0.77	Latex	Water	100, 200	Standard
SU1-S-W	SU1	0.77	Silicone	Water	100, 200	Standard
SU2-S-W	SU2	0.72	Silicone	Water	50, 100	Standard
SU2-S-O-L	SU2	0.70	Silicone	Oil	50, 100	Lubricated

Both oil- and water-saturated specimens were tested with silicone membranes. All oil-saturated specimens were tested with lubricated platens for comparison with a companion study on geogrid stabilization (Marx, Kumar, and Zornberg 2023).

Third, sand SU2 saturated with mineral oil was used to illustrate how shear band development can be quantified in terms of orientation, width, and inclination when transparent sand is combined with laser illumination (SU2-S-O-L). SU2 was used for the transparent sand because the particles were large enough for the full specimen to be transparent but small enough to meet the maximum particle size requirements of a triaxial test.

Image Analysis

The images of the two laser-illuminated sections were used to quantify shear bands that developed in the specimens. First, the images were preprocessed to be suitable for analysis. Next, the displacement across the images was analyzed using digital image correlation (DIC). From these displacement fields, the shear band width, orientation, and inclination were subsequently measured.

IMAGE PREPROCESSING

The image sensor of a color camera consists of a matrix of alternating red, green, and blue pixels. Consequently, the sensor captures a single channel image of discontinuous red, blue, and green (RGB) pixels. This discontinuous image is known as a raw image. Often, the raw image is converted in-camera to a conventional, three-channel (red, green, and blue) Joint Photographic Experts Group (JPEG) image. However, the JPEG conversion process may compress the texture of the images or clip the bright particle edges, resulting in a loss of information. Thus, for this study, the 12-bit raw images were manually processed into grayscale images to prevent loss of information.

Two stages of preprocessing operations were applied to the raw images, as visualized in **figure 5**. The first stage sharpened the particle edges, and the second stage corrected for image distortion. During the first stage, the raw images (**fig. 5*A***) were demosaiced into RGB channels using the Python library *rawpy* (Riechert, M., Cambridge, UK). These three channels (**fig. 5*B***) were subsequently averaged to produce a grayscale image (**fig. 5*C***).

The particle edges were significantly brighter than the particle centers. Consequently, the logarithm of the gray values was calculated to compress the dynamic range of the image (**fig. 5*D***). Finally, the effect of unequal illumination was removed using contrast limited histogram equalization (CLAHE). CLAHE brightens dark regions and darkens light regions of the image, such that the exposure across the image is consistent (Zuiderveld 1994). CLAHE was applied using the Python library *scikit-image* (van der Walt et al. 2014). A typical result of the operation is shown in **figure 5*E***.

In the second stage, the images were corrected for lens distortion, spatial offset, and the distortion resulting from capturing the images through the triaxial cell. This process is summarized in **figure 5*F*** and **5*G***. First, the images were cropped to the area occupied by the specimen. Next, the images were corrected for radial and tangential lens distortion (White, Take, and Bolton 2003). The lens distortion correction was calibrated from nine images of a calibration grid using the *OpenCV* (Bradski 2000) library for Python. Subsequently, other images captured at the same distance could be corrected for internal lens distortion using the *undistort* method of *OpenCV*.

During testing, movement of the camera might occur when the shutter of the camera is activated. At small displacements, misaligned images will increase the noise in the displacement measurements. By using the alignment frame, the images were aligned to a common reference using the *warpPerspective* routine of *OpenCV*.

The final distortion to correct was due to the cell wall acting as a negative meniscus lens. This was the most significant source of distortion and is the primary reason why specimens in a triaxial cell appear wider than their actual width. First, a model of the optical components of the imaging frame was developed. This allowed for the modeling of a ray of light originating at the laser plane, propagating through the oil and refracting from the cell wall to the camera (refer to Appendix A). By tracing the path of the light ray from the camera back to the laser

FIG. 5 Visualization of the image preprocessing (*A*) the raw image, (*B*) the demosaiced RGB image, (*C*) the equivalent gray image, (*D*) the log transformed image, (*E*) the equalized image (*F*) the sharpened image from E, cropped and (*G*) the final image, sharpened and corrected for distortion.

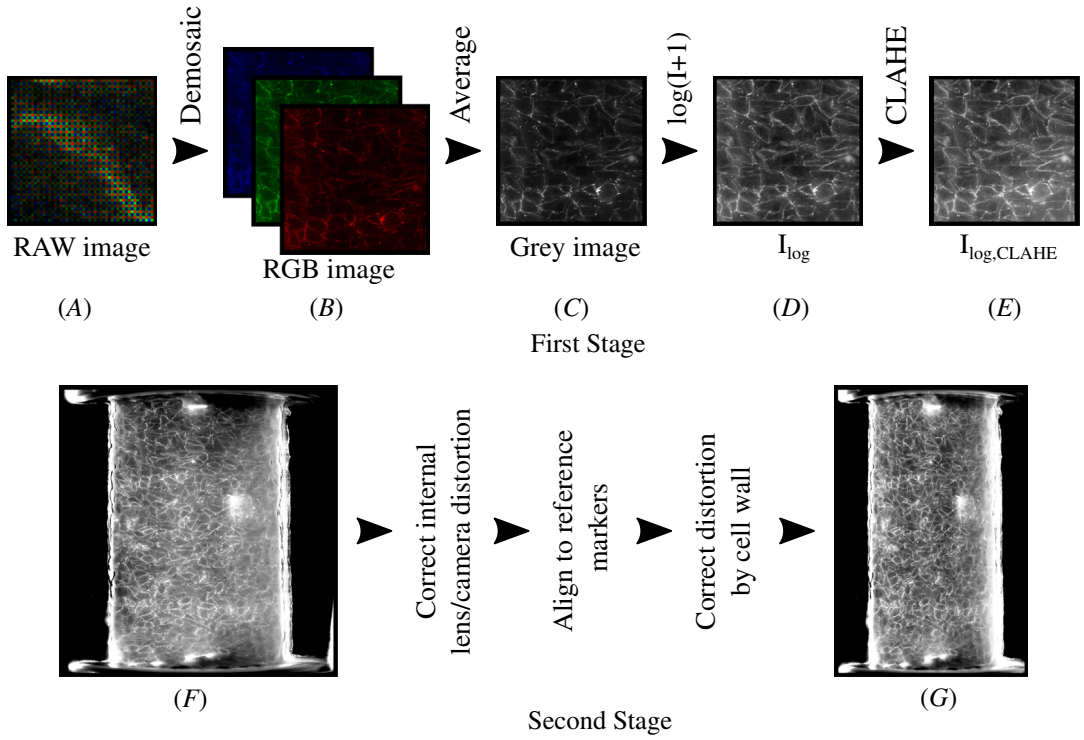

plane, the undistorted origin coordinate of the ray could be calculated. For this study, the ray-tracing method by Zhang et al. (2015) was used.

The area of the image used for analysis typically consisted of 11 million pixels. Ray tracing each of these pixels for each of the images would have been too computationally intensive. As an alternative, 64 pixels evenly spaced over the specimen were ray traced. Next, these 64 pixels were used to generate a surrogate surface that maps the distorted pixel coordinates to the undistorted pixel coordinates. A discussion on surrogate modeling can be found in Snyman and Wilke (2018). From the surrogate surface, the undistorted coordinates were interpolated for the remainder of the pixels. **Figure 5*G*** shows the corrected version of the distorted image in **figure 5*F***.

The refractive index of the different components, the cell diameter, the cell thickness, and the relative position of the different optical components were measured to calibrate the ray-tracing model. Because of the inherent uncertainty in these measurements, the uncertainty in the modeled, undistorted pixel coordinates was 0.41 mm (see Appendix A for a discussion on the uncertainty).

DIC

DIC is an optical measurement technique that can be used to measure the full field displacement of an imaged 2-D plane (Sutton, Orteu, and Schreier 2009). First, a reference image is divided into an array of patches (or subsets). Next, a target image is searched for the positions where the cross-correlations with these patches are maximized. With the new positions known, the displacement of the patches can be calculated. This field of displacements is used to calculate the strain fields in the image. Further information on applying the technique to geotechnical problems can be found in White, Take, and Bolton (2003) and Stanier et al. (2016).

For this study, the *GeoPIV-RG* software by Stanier et al. (2016) was used for the DIC analysis. *GeoPIV-RG* is DIC software based on the open-source software *Ncorr* (Blaber et al. 2015), which implements the reliability-guided method developed by Pan (2009). *GeoPIV-RG* considers first-order deformations of the subsets, which is critical for measuring the displacement of shear bands. Refer to Stanier et al. (2016) for further details of the implementation.

The images were first down-sampled by a factor of four because of computational limitations. Consequently, the images were in the order of 640 pixels wide and 1,050 pixels tall. The specimens were approximately 450 pixels wide by 900 pixels tall in the resized images. Subsets of 100 pixels in diameter (about 10 mm) were tracked during the DIC analyses. Thus, each subset encompassed around three particles each [i.e., three unique features as recommended by International Digital Image Correlation Society, Jones, and Iadicola (2018)]. To increase the spatial resolution of the measurements, the subsets were spaced 2.5 mm (approximately one particle diameter) apart. However, the resolution at which the DIC measurements could be reliably conducted was assumed to be closer to two particle diameters (i.e., 5.8 mm).

The DIC results were postprocessed to filter poorly correlated patches and stray displacement vectors. Next, biharmonic spline interpolation was used to interpolate a continuous displacement field from the filtered DIC results. This displacement field was then used as input to the *GeoPIV-RG* strain routine.

Compression of the lubricated ends during the test results in unreliable external measurements of axial deformation (Clayton and Khatrush 1986). Consequently, local strain measurements were necessary for the specimens tested with lubricated ends (series SU2-S-O-L). For these specimens the axial strain was calculated from the DIC displacement measurements (Marx and Zornberg 2022). The difference in average vertical displacement between two rows of subsets was used for the strain calculation: one row was at the top of the specimen, and the other was at the bottom.

SHEAR BAND QUANTIFICATION

From the DIC measurements, two sequences of intersecting 2-D shear-strain fields were obtained for each specimen. For each timestep, the 2-D strain fields were orientated in 3-D based on the relative position of the lasers, as shown in **figure 6**. The figure is colored to show the incremental shear strain that accumulated in the specimen during a typical slip event. In addition, the inclination and relative magnitude of the major, intermediate, and minor principal axes for the strain concentration (i.e., the shear band) is indicated. The calculation of the principal axes of the strain concentration is discussed in the next section.

Definition of the Principal Axes

The major principal axis of the shear band is the direction of the minimum variance in the strain field. Thus, the orientation of the major principal axis can be calculated from the covariance matrix of the strain field. In two dimensions, the covariance matrix of an image defines the variation in pixel intensity along a combination of two axes (e.g., $x - y$, $x - x$, or $y - y$). The eigenvectors of this covariance matrix are aligned with the directions in which the pixel intensity varies the most and the least. These are the principal axes of the image. In the case where the image represents incremental shear strain, the major principal axis is parallel to the direction of the shear band (Nguyen and Amon 2016). This calculation can be extended to three dimensions, as shown in Appendix B. The resulting three eigenvectors correspond to the major, intermediate, and minor principal axes of the image.

The covariance matrix of the data, and by extension the principal axes, is a function of not only the incremental shear strain (γ_{inc}) but also the spatial distribution of the points. If the points are concentrated along a given direction (i.e., the vertical), the major principal axis will tend to align with that direction. Consequently, the principal axes were calculated considering only the pixels that formed part of a shear band.

To isolate the shear band from the remainder of the image, the boundary strain had to be determined. The distribution of strain that developed during the slip event shown in **figure 6** is shown in **figure 7**. It was assumed that the distribution consisted of the sum of two Gaussian distributions: one representing the shear band (μ_2, σ_2) and another representing the remainder of the image (μ_1, σ_1). The intersection of the two distributions, γ_{sb}, was

FIG. 6

Three-dimensional representation of the incremental shear strain in a specimen during a slip event.

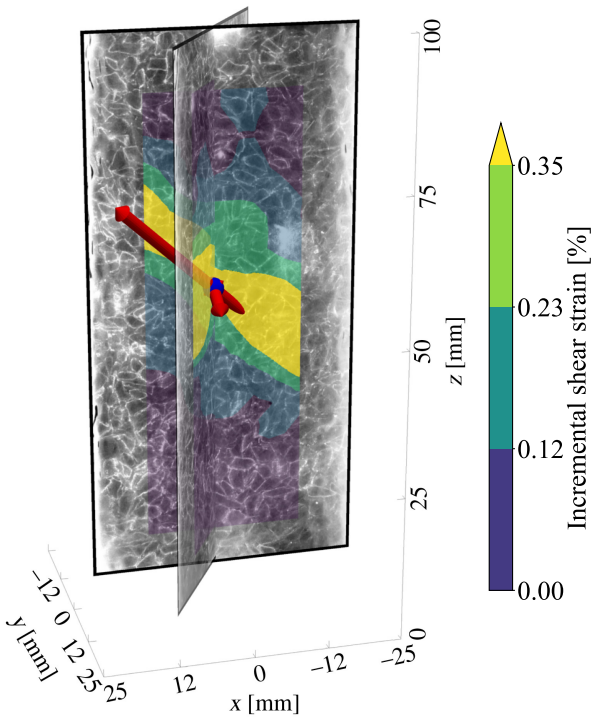

assumed to be the boundary of the shear band. The two Gaussian distributions shown in figure 7 were fitted using the Python library *scikit-learn* (Pedregosa et al. 2011).

Figure 8 is a 2-D projection of figure 6. The 3-D data points are projected onto a plane perpendicular to the intermediate principal axis. In addition, contours of γ_{sb} and μ_2 are indicated. The principal axis calculated from the points greater than γ_{sb} was still sensitive to the spatial distribution of the data. Thus, μ_2 was used as the boundary for the calculations of the principal axes. The corresponding principal axes are indicated in figure 8 (the intermediate principal axis projects out of the page).

Using the eigenvalues, the degree of anisotropy of the slip event was calculated as follows: $a_{13} = 1 - \lambda_1/\lambda_3$, where λ_1 is the eigenvalue associated with the major principal axis and λ_3 is the the eigenvalue associated with the minor principal axis (Nguyen and Amon 2016). A value of 0 represents an isotropic strain distribution (i.e., a shear band has not formed), whereas 1 implies a highly anisotropic strain distribution.

Calculation of the Inclination, Orientation, and Width of the Shear Bands

The inclination of a shear band (θ) was defined as the angle between the major principal axes of the shear band and the plane of the minor principal stress applied to the specimen (Kawamoto et al. 2018), i.e., the *xy* plane in the triaxial specimen shown in figure 6 (also see the inset to fig. 8). The orientation of the shear bands was the angle of the projection of the principal axis on the *xy* plane.

To calculate the width of the shear bands it was assumed that the distribution of the shear strain is uniform along the breadth of the shear band (i.e., along the intermediate principal axis). Consequently, the median of the 3-D incremental shear-strain measurements along the intermediate principal axis was calculated. This produced a distribution similar to the one shown in figure 8.

Next, it was assumed that the distribution of shear strain is uniform along the length of the shear band (i.e., along the major principal axis). By now calculating the median along the major principal axis as well, a

FIG. 7

Distributions of incremental shear strain during a slip event.

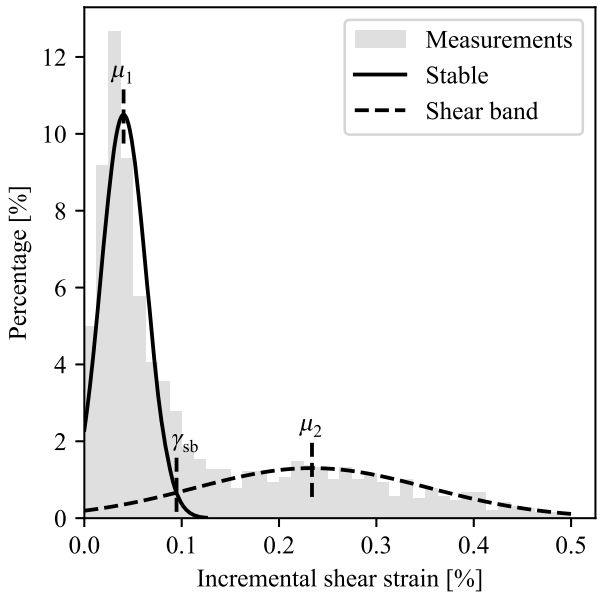

representative shear-strain distribution was calculated for the shear band. An example of such a representative distribution is shown in figure 9. In addition, the μ_1, μ_2, and γ_{sb}, as defined in figure 7, is indicated.

The representative shear-strain distribution in figure 9 was assumed to be Gaussian distribution shaped. In signal processing, the full width at half maximum (FWHM) is often used to describe the width of an impulse signal such as a Gaussian distribution (Weik 2001). In the past, the FWHM has also been used to quantify the width of a shear band (Nguyen and Amon 2016). However, a shear band encompasses the full region of localized strain. Thus, for this study, the width was measured at the base of the distribution. Specifically, at the points on the shoulders of the Gaussian distribution where the curvature is a maximum. This distance, w, is indicated in figure 9.

FIG. 8

Incremental shear strain during the slip event shown in figure 6 projected on a plane perpendicular to the intermediate principal axis.

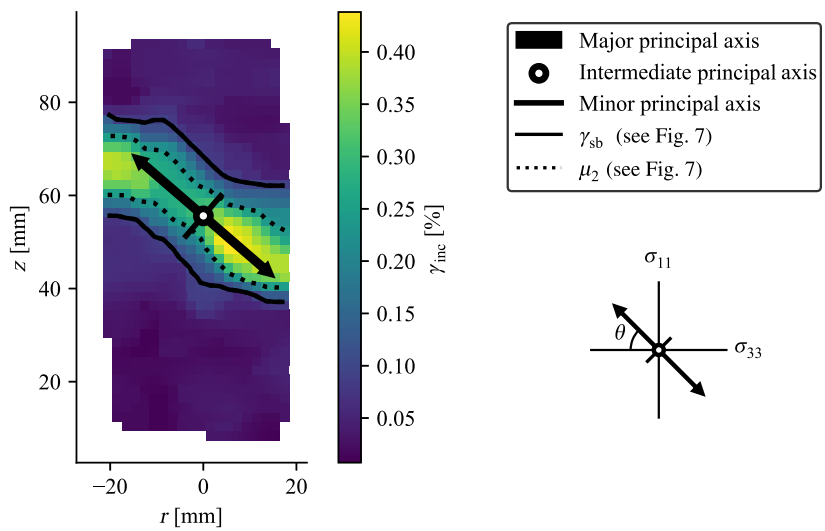

FIG. 9

Representative distribution of the shear strain that incremented over the slip event in figure 6.

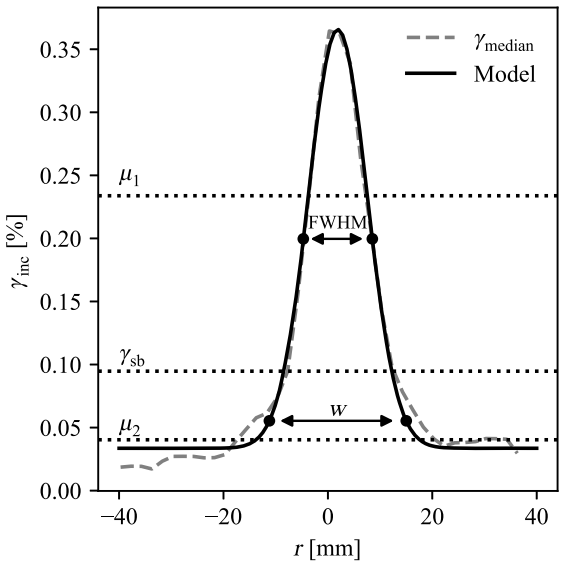

Results

EQUIVALENCY OF LATEX AND SILICONE MEMBRANES

In figure 10, the stress-strain responses of the specimens of SU1, tested with conventional, 0.7-mm thick latex membranes (SU1-L-W), are compared to SU1 tested with the silicone membranes (SU1-S-W). In general, the deviatoric stress-axial strain response of the two series were comparable. The volumetric behavior was also similar for the two membranes. The peak, secant friction angles measured with the two membranes differed within 0.5° (refer to Table 3). The angles of dilation differed with 1.8° at 100 kPa and 1.3° at 200 kPa. Thus, the mechanical response of the sand was invariant to the type of membrane used. The silicone and the latex membranes can therefore be considered equivalent for the purpose of triaxial testing.

STRESS-STRAIN RESPONSE OF SU2

The stress-strain curves for the SU2, saturated with both oil (SU2-S-O-L) and water (SU2-S-W-L), are shown in figure 11 for two different confining stresses. The stress-strain curves presented in figure 11 differ from the expected behavior of a dense, angular, cohesionless material with a dilative volumetric response in three ways: (1) the occurrence of slip-stick behavior, (2) continued dilation at high axial strain, and (3) a lack of strain hardening up to a peak followed by strain softening for the oil-saturated specimens.

At low strains, there is little difference in the response of oil- and water-saturated specimens. However, once slip-stick occurs, the behavior changes. For both the oil-saturated specimens shown in figure 11, slip-stick behavior initiated at the onset of plastic behavior, as reported by Alshibli and Roussel (2006) and Ezzein and Bathurst (2011). In the results reported by Carvalho et al. (2015), slip-stick occurred only after the deviatoric stress has peaked. The difference may be due to the high rate of shear in that study that suppressed slip-stick behavior (Ozbay and Cabalar 2016). Because of the smooth, lubricated interfaces between the fused quartz particles, interlock is limited. Thus, chains of load bearing particles can only grow up to a limited length and number before they buckle brittlely resulting in the "slip" events.

The angle of dilation decreased from 25.0° at 50 kPa confining stress to 21.8° at 100 kPa confining stress for the oil-saturated specimens (see Table 4). Large angles of dilation appear to be characteristic of triaxial tests done on both water- and oil-saturated fused quartz (Carvalho et al. 2015; Ezzein and Bathurst 2011). For

FIG. 10

Comparison of the stress-strain response of SU1 tested with both silicone membranes and conventional latex membranes.

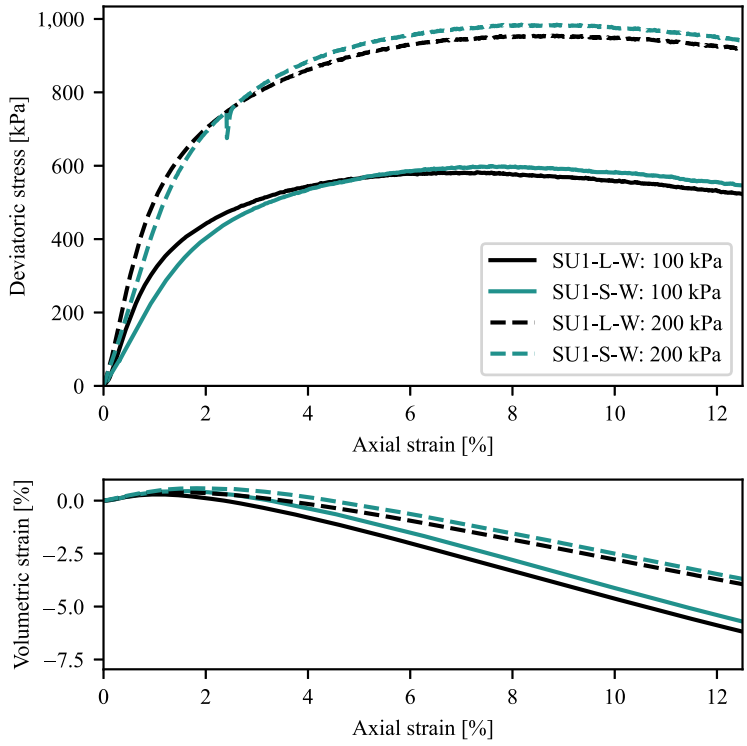

TABLE 3

Comparison of the peak, secant friction angles and angles of dilation measured for SU1 tested in latex and silicone membranes, saturated with water

		Peak, Secant Friction Angle, °		Angle of Dilation, °	
Series Name	Membrane Material	$\sigma_3' = 100$ kPa	$\sigma_3' = 200$ kPa	$\sigma_3' = 100$ kPa	$\sigma_3' = 200$ kPa
SU1-L-W	Latex	48.6	45.4	43.2	29.1
SU1-S-W	Silicone	48.9	45.8	45.0	30.4

the water-saturated specimens the angles of dilation were 35.1° and 28.9° at confining stresses of 50 kPa and 100 kPa, respectively. Ezzein and Bathurst (2011) similarly measured a decrease in dilation as the lubrication due to the pore fluid increased from air to water to oil. The continued dilation at large axial strain indicates that global strain localization has not yet occurred, and thus critical state has not been achieved.

The peak, secant friction angles of the oil and water-saturated specimens of SU2 are compared in **Table 4**. The peak secant friction angle was calculated at the maximum σ_1'/σ_3' ratio. For the oil-saturated specimens of SU2 the peak, secant friction angle was 43.1° at a confining stress of 50 kPa and 42.7° at a confining stress of 100 kPa. These friction angles are of a similar range to the values reported by Ezzein and Bathurst (2011), Carvalho et al. (2015), Derksen, Ziegler, and Fuentes (2021) and others. For the water-saturated specimens the peak secant friction angles increased because of the lower lubrication by water compared to oil and was 46.8° and 45.67° for the 50 kPa and 100 kPa confining stresses respectively. A lower peak strength (i.e., reduced strain softening), for oil-saturated fused quartz was also reported by Ezzein and Bathurst (2011) and Carvalho et al. (2015). However, the difference in peak strength between water and oil-saturated specimens was not as severe as shown in **figure 11**.

FIG. 11

Comparison of stress-strain response for oil and water-saturated specimens of sand SU2.

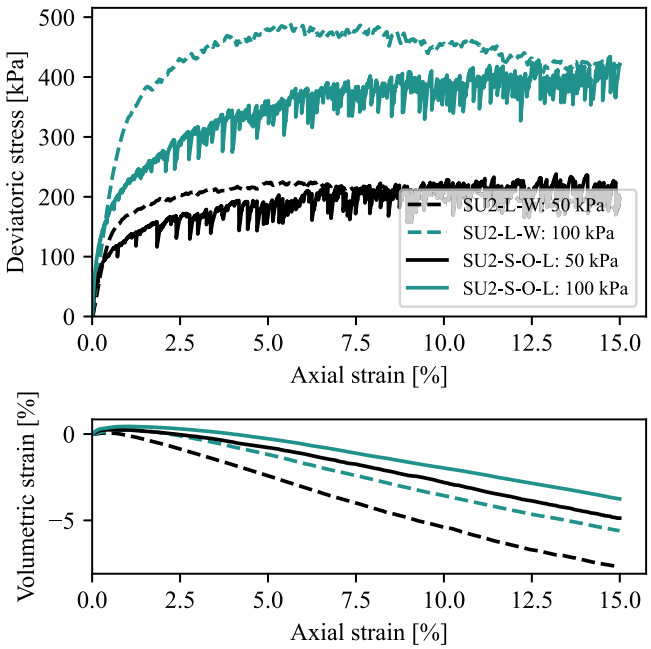

TABLE 4

Comparison of the peak, secant friction angles and angles of dilation measured for SU2 for oil and water saturation

		Peak, Secant Friction Angle, °		Large Strain, Secant Friction Angle, °		Angle of Dilation, °	
Series Name	Saturating Fluid	$\sigma_3' = 50$ kPa	$\sigma_3' = 100$ kPa	$\sigma_3' = 50$ kPa	$\sigma_3' = 100$ kPa	$\sigma_3' = 50$ kPa	$\sigma_3' = 100$ kPa
SU2-S-W	Water	46.8	45.7	40.3	43.2	35.1	28.9
SU2-S-O-L	Oil	43.1	42.8	42.3	42.4	25.0	21.8

The lack of strain softening, and the severe, continued dilation that was observed for the soil saturated specimens is similar to the discrete element simulations by Iwashita and Oda (1998) where particles were restricted to slide, and not rotate, during shear. Similarly, in oil-saturated fused quartz, sliding is the predominant mechanism of deformation because of the oil lubricating the smooth fused quartz surfaces.

Both oil- and water-lubricated specimens eventually converged to the same large strain strength. The large strain friction angle was calculated for the peak deviatoric stress between 14.5 % and 15 % axial strain. The peak value over this axial strain increment was assumed to be representative of the large strain strength, rather than local minima that correspond to slip events. The large strain secant friction angle was comparable between the oil- and water-saturated specimens. For the oil-saturated specimens, there was little difference between the peak and large strain strengths (i.e., almost no strain softening occurred).

TYPICAL EXAMPLES OF STRAIN LOCALIZATION IN TRANSPARENT SAND

Typical examples of the strain localization that occurred during the slip events of SU2-S-O-L tested at 50 kPa confining stress are shown in figure 12. In figure 12*A*, the axial strain at which images were captured during the test are indicated on the stress-strain curve. Figure 12*B*–*D* shows the incremental shear strain that has developed between three different pairs of frames (images). The strain field shown is projected perpendicular to the major principal axis of the shear band. Each pair of frames are spaced approximately 0.025 % strain apart.

FIG. 12 Examples of strain localization measured for SU2-S-O-L at 50 kPa: (*A*) excerpt of the stress-strain results indicating when images were captured, (*B-D*) shear strain that developed over the specified axial strain increment, and (*E-G*) cumulative shear strain up to the specified axial strain.

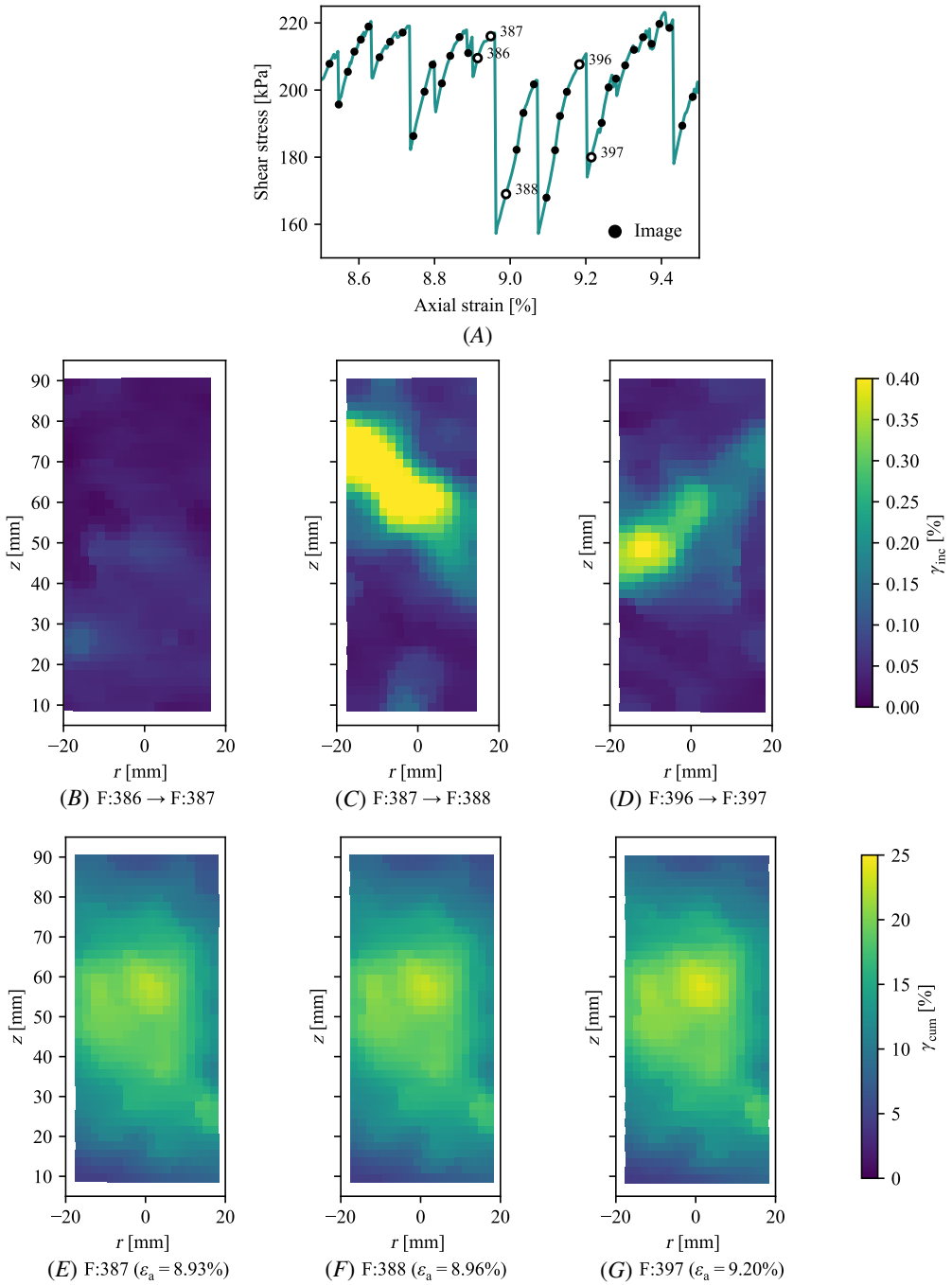

Frames 386 and 387 (fig. 12*B*) were captured during a "stick" event; thus, no strain localization is observed. Frames 387 and 388 (fig. 12*C*) and Frames 396 and 397 (fig. 12*D*) both bisect "slip" events. Consequently, severe localization of shear strain is apparent. The alternating inclination of the strain localization indicates that a single, defined shear band did not form. Figure 12*E*–*G* shows the shear strain that has accumulated in the specimen up to a given frame (axial strain). Consistent with alternating inclinations of the shear bands shown in figure 12*B*–*D*, the cumulative shear strain was homogeneous even after 9 % axial strain. Thus, the localization occurred so quickly that the deformation appeared uniform in composite.

SHEAR BAND ORIENTATION, STRAIN MAGNITUDE, WIDTH, AND INCLINATION

During each of the slip events shown in figure 11*A*, a shear band formed in the specimen. Approximately 100 events occurred during each test. However, only the shear bands that developed within the sector between the two laser-illuminated sections could accurately be quantified. Because the cameras were placed at an angle of 60° to each other, it was assumed that 33 % of the shear bands that developed intersected both laser-illuminated planes.

For each of the slip events, the principal axis of the strain concentration was calculated. For the subsequent analysis, only slip events that met the following criteria were considered: (*A*) the orientation of the major principal axis falls inside the observable sector and (*B*) the degree of anisotropy between the principal axes met the following criteria: (i) $a_{13} \geq 0.8$, (ii) $a_{13} \geq 0.5$, and (iii) $a_{23} \geq 0.5$. Twenty-nine percent of slip events of the 50 kPa test met the criteria and 27 % of the 100 kPa test met the criteria.

The orientations of the observed shear bands on the *xy* plane (fig. 6) for the 50 kPa test are shown in figure 13 as a function of the deviatoric strain. The specimen did not fail along a single failure plane as demonstrated in figure 12. Rather, a family of conjugate shear bands developed, alternating in orientation as the deviatoric strain increased. The orientation of the shear bands for both tests is summarized in figure 14. For both confining stresses tested, the observable orientations were equally distributed between 60°–120° and 240°–300°. Presumably, the other 66 % of slip events were equally distributed through the remainder of the specimen. This family of conjugate shear bands that developed was reflected in the specimens failing in a bulging mode.

The probability distributions of the widths of shear bands that formed in each of the three tests of test series SU2-S-O-L are shown in figure 15. A distribution of values was measured because of the inherent variability in shear band development and the noise associated with reconstructing a 3-D structure from two 2-D observations.

Median widths of 24.6 mm ($8.6 \times D_{50}$) and 32.8 mm ($11.5 \times D_{50}$) were measured for the 50 kPa and 100 kPa tests, respectively. In general, the shear band widths reported in literature ranged between 8 and 16 $\cdot D_{50}$ across different sands and densities (Alshibli and Sture 1999; Amon et al. 2012; Bridgwater 1980; Oda and Kazama 1998; Rattez et al. 2022; Roscoe 1970; Saada et al. 1999; Scrapelli and Wood 1982).

The probability distribution of the inclination of the shear bands relative to the plane of the minor principal stress is shown in figure 16. The median inclination of the shear bands increased from 55° to 65.5° as the

FIG. 13

Orientation of the shear bands that developed in SU2-S-O-L at 50 kPa at a given axial strain.

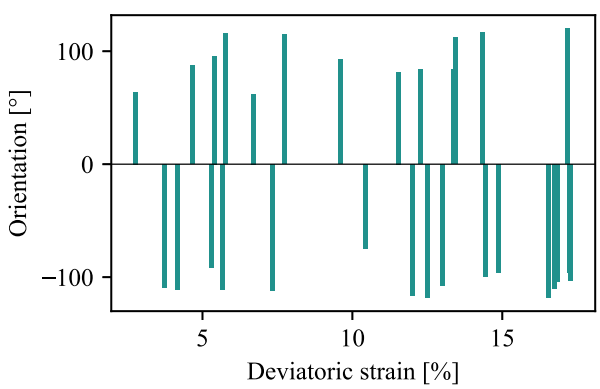

FIG. 14

Shear band orientation as a function of confining stress for test series SU2-S-O-L.

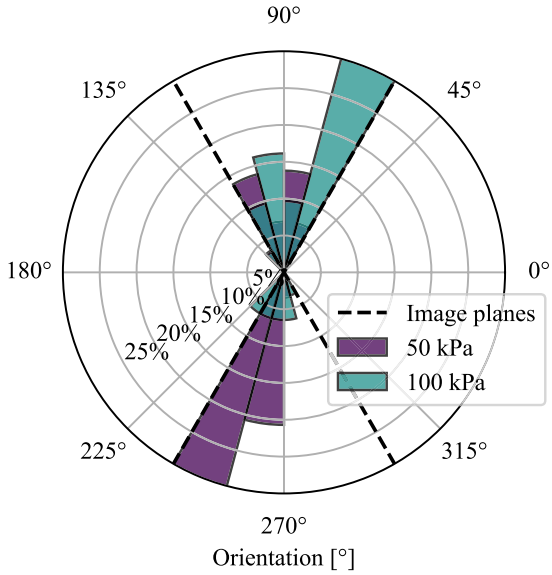

FIG. 15

Probability distribution of shear band width for test series SU2-S-O-L.

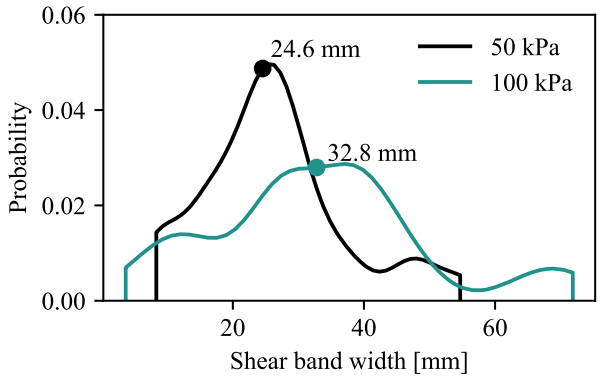

FIG. 16

Probability distribution of shear band inclination for test series SU2-S-O-L.

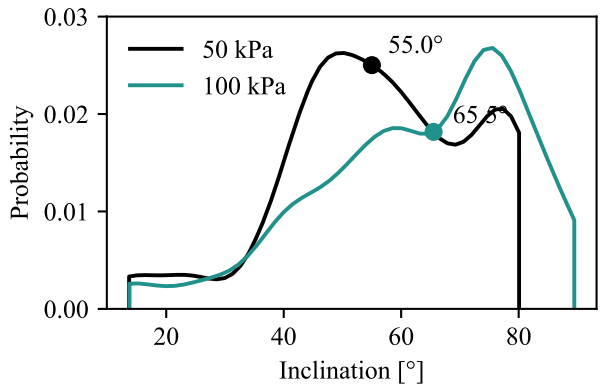

confining stress increased. This is contrary to the theoretical models based on the theories by Coulomb ($\theta = 45° + \phi'/2$), Roscoe (1970) ($\theta = 45° + \psi'/2$), and Arthur et al. (1977), and Vardoulakis (1980) ($\theta \approx 45° + (\phi' + \psi')/4$. In these models the inclination of the shear bands is directly proportional to either the friction angle or the dilation angle, or both. Because both ϕ' and ψ' tend to decrease with confining stress, the models would suggest θ should decrease with confining stress. However, the measured increase in the inclination of the shear band with confining stress is consistent with the experimental results presented by (Alshibli and Sture 2000; Desrues and Viggiani 2004; Vardoulakis and Sulem 1995).

Conclusions

This work presented a novel technique to measure the development of shear bands in triaxial specimens of transparent sand. Displacement fields were measured along two intersection sections through the specimens. The displacements were measured by applying DIC to images of the sections. Subsequently, the strain along the sections was calculated. From the two 2-D strain fields, it was possible to orientate the shear band in three dimensions. The major, intermediate and minor principal axes of the shear bands were calculated from the 3-D reconstruction. In addition, the orientation, width, inclination, and maximum strain in the shear bands could be calculated.

Three sets of triaxial testing results were presented. The first was a comparative study of traditional latex membranes and the custom silicone membranes developed as part of this study. Similar stress-strain responses of fine-grained fused quartz were measured in tests done using both types of membranes. Thus, these custom silicone membranes are valid alternatives to conventional triaxial membranes that have greater chemical resistance and are transparent.

In the second set of test results, the stress-strain response of oil-saturated fused quartz (transparent sand) was compared to that of water-saturated fused quartz. At both small and large axial strain, the two sets of results converged. However, the water-saturated specimens strain hardened at a greater rate, resulting in increased volumetric strain. In addition, strain softening occurred only for the water-saturated specimens.

The final set of results illustrated the method used to measure the shear bands. For both specimens tested, the orientations of the shear bands on the *xy* plane were equally distributed between the observable directions. Thus, a family of conjugate shear bands were measured. The family of conjugate shear bands that developed, rather than a discrete slip, reflected in a bulging mode of failure. The width of the shear bands was between $8.6 \cdot D_{50}$ to $11.5 \cdot D_{50}$ across the confining stresses evaluated. Finally, the inclination of the shear bands increased with confining stress. This behavior did not correspond to either the Mohr-Coulomb model or the Roscoe model. However, the results are consistent with other experimental measurements of shear band inclination.

Appendix A: Ray-Tracing Uncertainty Calculations

Uncertainty inherent to the optical properties of the experimental setup resulted in uncertainty of the ray-traced, undistorted coordinates. This uncertainty was quantified using the principle of propagation of uncertainty. Specifically, the sequential method (also referred to as the function method) was implemented (Hughes and Hase 2010).

Consider the undistorted coordinate x_U that is a function of the parameters defined in **figure A.1** and listed in **Table A.1**:

$$x_U = f(x_D, \Delta y_1, y_c, \Delta x_L, \kappa, \omega, t, D, \ldots) \tag{A.1}$$

where f is the ray-tracing method discussed by Zhang et al. (2015). Next, the individual contribution of a parameter (e.g., κ) to the uncertainty in x_U is as follows:

FIG. A.1

Factors contributing to the uncertainty in the accuracy of the analytical ray tracing.

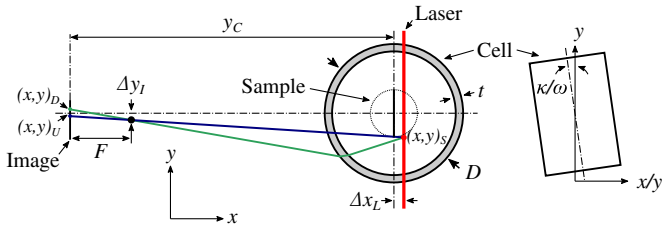

$$\delta(x_U)_\kappa = (x_U)_\kappa^+ - (x_U)_0 \tag{A.2}$$

where $(x_U)_0$ is the undistorted coordinate calculated with the default values for the parameters and $(x_U)_\kappa^+$ is the value of x_U for a perturbation in κ.

$$(x_U)_\kappa^+ = f(x_D, \Delta y_1, y_c, \Delta x_L, \kappa + \delta\kappa, \omega, t, D, \ldots) \tag{A.3}$$

where $\delta\kappa$ is the uncertainty in the measurement of κ. The total uncertainty was the measurement of x_U because of each of the parameters can then be calculated as follows:

$$\delta x_U = [(\delta(x_U)_{x_D})^2 + (\delta(x_U)_{\Delta y_1})^2 + \ldots + (\delta(x_U)_\kappa)^2 + \ldots]^{\frac{1}{2}} \tag{A.4}$$

The propagation of error method was applied to calculate the uncertainty in $(x,y)_U$ for nine points distributed evenly over the image. The parameters used in the ray-tracing analysis, their values, and the associated uncertainty are shown in Table 5. In addition, the contribution of a variable to the total uncertainty, reported as the maximum of the nine points, is also shown. The contribution to the total uncertainty was defined as the absolute distance of the uncertainty in x and y: $\sqrt{\delta x_U^2 + \delta y_U^2}$. Consequently, the total uncertainty was 0.43 mm.

TABLE A.1

Uncertainty in variables for the ray-tracing analysis

Variable	Description	Value	Uncertainty	Maximum Contribution to Total Uncertainty, mm
F_1	Factor to convert image pixels to millimeters based on a measuring tape on the cell wall	44.4 mm	0.25 mm	0.279
Δy_1	In-plane offset of camera from the center of the cell	0.2 mm	0.04 mm	0.212
$D/2$	Cell radius	63.2 mm	0.05 mm	0.006
κ	In-plane rotation of the cell	0	0.5°	0.150
ω	Out of plane rotation of the cell	0	0.5°	0.141
t	Thickness of the cell wall	6.38 mm	0.1 mm	0.000
Δx_L	Offset of the laser from the center of the cell	−0.6 mm	0.75 mm	0.112
n_{FQ}	Refractive index of the fused quartz and oil mixture	1.46	0.005	0.067
F	Focal distance of the lens	53.7 mm	0.1 mm	0.015
n_A	Refractive index of the acrylic	1.49	0	0
F_1	Calibration factor to calculate the actual size of the pixels on the sensor	0.00414	0	0
Total	…	…	…	0.41

Appendix B: Calculation of Principal Axes in Three Dimensions

To calculate the principal axis in three dimensions, the central moments of the data points were first calculated as follows:

$$\mu_{pqr} = \sum_x \sum_y \sum_z (x - \bar{x})^p (y - \bar{y})^q (z - \bar{z})^r f(x, y, z) \tag{B.1}$$

where $(\bar{x}, \bar{y}, \bar{z})$ is the centroid of the data points and $f(x, y, z)$ is the strain value at that coordinate.

Next, the covariance matrix was calculated:

$$cov[f(x, y, z)] = \begin{bmatrix} \mu'_{200} & \mu'_{110} & \mu'_{101} \\ \mu'_{110} & \mu'_{020} & \mu'_{011} \\ \mu'_{101} & \mu'_{011} & \mu'_{002} \end{bmatrix} \tag{B.2}$$

where $\mu'_{200} = \mu_{(p=2,q=0,r=0)} / \mu_{(p=0,q=0,r=0)}$, $\mu'_{110} = \mu_{(p=1,q=1,r=0)} / \mu_{(p=0,q=0,r=0)}$, and $\mu'_{pqr} = \mu_{pqr} / \mu_{(p=0,q=0,r=0)}$.

Finally, the eigenvalues and eigenvectors of the covariance matrix were calculated. The eigenvector corresponding to the largest eigenvalue is the major principal axis.

ACKNOWLEDGMENTS

The authors thank Tensar International Corporation for the financial assistance provided for the study. Opinions expressed and conclusions presented are solely those of the authors. The first author is grateful for the support provided by a Harrington Dissertation Fellowship.

References

Alshibli, K. A. and L. E. Roussel. 2006. "Experimental Investigation of Slip-Stick Behaviour in Granular Materials." *International Journal for Numerical and Analytical Methods in Geomechanics* 30, no. 14 (December): 1391–1407. https://doi.org/10.1002/nag.517

Alshibli, K. A. and S. Sture. 1999. "Sand Shear Band Thickness Measurements by Digital Imaging Techniques." *Journal of Computing in Civil Engineering* 13, no. 2 (April): 103–109. https://doi.org/10.1061/(ASCE)0887-3801(1999)13:2(103)

Alshibli, K. A. and S. Sture. 2000. "Shear Band Formation in Plane Strain Experiments of Sand." *Journal of Geotechnical and Geoenvironmental Engineering* 126, no. 6 (June): 495–503. https://doi.org/10.1061/(ASCE)1090-0241(2000)126:6(495)

Amon, A., V. B. Nguyen, A. Bruand, J. Crassous, and E. Clément. 2012. "Hot Spots in an Athermal System." *Physical Review Letters* 108, no. 13 (March): 135502. https://doi.org/10.1103/PhysRevLett.108.135502

Arthur, J. R. F., T. Dunstan, Q. A. J. L. Al-Ani, and A. Assadi. 1977. "Plastic Deformation and Failure in Granular Media." *Géotechnique* 27, no. 1 (March): 53–74. https://doi.org/10.1680/geot.1977.27.1.53

ASTM International. 2016. *Standard Test Methods for Maximum Index Density and Unit Weight of Soils Using a Vibratory Table*. ASTM D4253-16. West Conshohocken, PA: ASTM International, approved March 1, 2016. https://doi.org/10.1520/D4253-16E01

ASTM International. 2016. *Standard Test Methods for Minimum Index Density and Unit Weight of Soils and Calculation of Relative Density*. ASTM D4254-16. West Conshohocken, PA: ASTM International, approved March 1, 2016. https://doi.org/10.1520/D4254-16

Blaber, J., B. Adair, and A. Antoniou. 2015. "Ncorr: Open-Source 2D Digital Image Correlation Matlab Software." *Experimental Mechanics* 55, no. 6 (July): 1105–1122. https://doi.org/10.1007/s11340-015-0009-1

Bradski, G. 2000. "The OpenCV Library." *Dr. Dobb's Journal of Software Tools* 20, no. 11 (November): 120–125.

Bridgwater, J. 1980. "On the Width of Failure Zones." *Géotechnique* 30, no. 4 (December): 533–536. https://doi.org/10.1680/geot.1980.30.4.533

Carvalho, T., E. Suescun-Florez, M. Omidvar, and M. Iskander. 2015. "A Nonviscous Water-Based Pore Fluid for Modeling with Transparent Soils." *Geotechnical Testing Journal* 38, no. 5 (September): 805–811. https://doi.org/10.1520/GTJ20140278

Cheng, Z. and J. Wang. 2018. "Experimental Investigation of Inter-particle Contact Evolution of Sheared Granular Materials Using X-ray Micro-tomography." *Soils and Foundations* 58, no. 6 (December): 1492–1510. https://doi.org/10.1016/j.sandf.2018.08.008

Clayton, C. R. I. and S. A. Khatrush. 1986. "A New Device for Measuring Local Axial Strains on Triaxial Specimens." *Géotechnique* 36, no. 4 (December): 593–597. https://doi.org/10.1680/geot.1986.36.4.593

Derksen, J., M. Ziegler, and R. Fuentes. 2021. "Geogrid-Soil Interaction: A New Conceptual Model and Testing Apparatus." *Geotextiles and Geomembranes* 49, no. 5 (October): 1393–1406. https://doi.org/10.1016/j.geotexmem.2021.05.011

Desrues, J. and G. Viggiani. 2004. "Strain Localization in Sand: An Overview of the Experimental Results Obtained in Grenoble Using Stereophotogrammetry." *International Journal for Numerical and Analytical Methods in Geomechanics* 28, no. 4 (April): 279–321. https://doi.org/10.1002/nag.338

Duncan, J. M. and H. B. Seed. 1967. "Corrections for Strength Test Data." *Journal of the Soil Mechanics and Foundations Division* 93, no. 5 (September): 121–137. https://doi.org/10.1061/JSFEAQ.0001015

Ezzein, F. M. and R. J. Bathurst. 2011. "A Transparent Sand for Geotechnical Laboratory Modeling." *Geotechnical Testing Journal* 34, no. 6 (November): 590–601. https://doi.org/10.1520/GTJ103808

Galaz, B., D. Espíndola, and F. Melo. 2018. "Amplification of Stick-Slip Events through Lubricated Contacts in Consolidated Granular Media." *Physical Review E* 98, no. 4 (October): 042907. https://doi.org/10.1103/PhysRevE.98.042907

Head, K. H. 2014. *Manual of Soil Laboratory Testing*. 3rd ed. Dunbeath, UK: Whittles Publishing.

Hecht, E. 2016. *Optics Global Edition*. 5th ed. London: Pearson.

Henkel, D. J. and G. D. Gilbert. 1952. "The Effect Measured of the Rubber Membrane on the Triaxial Compression Strength of Clay Samples." *Géotechnique* 3, no. 1 (March): 20–29. https://doi.org/10.1680/geot.1952.3.1.20

Hughes, I. and T. P. A. Hase. 2010. *Measurements and Their Uncertainties: A Practical Guide to Modern Error Analysis*. 1st ed. Oxford, UK: Oxford University Press.

International Digital Image Correlation Society, E. M. C. Jones, and M. A. Iadicola, eds. 2018. *A Good Practices Guide for Digital Image Correlation*. Irmo, SC: International Digital Image Correlation and Society. https://doi.org/10.32720/idics/gpg.ed1/print.format.

Iskander, M., R. J. Bathurst, and M. Omidvar. 2015. "Past, Present, and Future of Transparent Soils." *Geotechnical Testing Journal* 38, no. 5 (September): 557–573. https://doi.org/10.1520/GTJ20150079

Iwashita, K. and M. Oda. 1998. "Rolling Resistance at Contacts in Simulation of Shear Band Development by DEM." *Journal of Engineering Mechanics* 124, no. 3 (March): 285–292. https://doi.org/10.1061/(ASCE)0733-9399(1998)124:3(285)

Kawamoto, R., E. Andò, G. Viggiani, and J. E. Andrade. 2018. "All You Need is Shape: Predicting Shear Banding in Sand with LS-DEM." *Journal of the Mechanics and Physics of Solids* 111: 375–392. https://doi.org/10.1016/j.jmps.2017.10.003

La Rochelle, P., S. Leroueil, B. Trak, L. Blais-Leroux, and F. Tavenas. 1988. "Observational Approach to Membrane and Area Corrections in Triaxial Tests." In *Advanced Triaxial Testing of Soil and Rock*, edited by R. T. Donaghe, R. C. Chaney, and M. L. Silver, 715–731. West Conshohocken, PA: ASTM International. https://doi.org/10.1520/STP29110S

Leib, A. R., A. Sharma, and D. Penumadu. 2021. "Visualization of Localized Deformations of Sand in Drained Triaxial Compression Using Digital Image Correlation." *Geotechnical Testing Journal* 44, no. 3 (May): 782–798. https://doi.org/10.1520/GTJ20190096

Li, L., X. Zhang, G. Chen, and R. Lytton. 2016. "Measuring Unsaturated Soil Deformations during Triaxial Testing Using a Photogrammetry-Based Method." *Canadian Geotechnical Journal* 53, no. 3 (March): 472–489. https://doi.org/10.1139/cgj-2015-0038

Marx, D. H. and J. G. Zornberg. 2022. "Shear Band Measurement in Transparent Sand." In *Proceedings of the 20th International Conference on Soil Mechanics and Geotechnical Engineering*, 163–168. Sydney, Australia: Australian Geomechanics Society.

Marx, D. H., K. Kumar, and J. G. Zornberg. 2023. "Quantification of Geogrid Lateral Restraint Using Transparent Sand and Deep Learning-Based Image Segmentation." *Geotextiles and Geomembranes* 51, no. 5 (October): 53–69. https://doi.org/10.1016/j.geotexmem.2023.04.004

Nemat-Nasser, S. and N. Okada. 2001. "Radiographic and Microscopic Observation of Shear Bands in Granular Materials." *Géotechnique* 51, no. 9 (November): 753–765. https://doi.org/10.1680/geot.2001.51.9.753

Nguyen, T. B. and A. Amon. 2016. "Experimental Study of Shear Band Formation: Bifurcation and Localization." *Europhysics Letters* 116, no. 2 (October): 28007. https://doi.org/10.1209/0295-5075/116/28007

Oda, M. and H. Kazama. 1998. "Microstructure of Shear Bands and Its Relation to the Mechanisms of Dilatancy and Failure of Dense Granular Soils." *Géotechnique* 48, no. 4 (August): 465–481. https://doi.org/10.1680/geot.1998.48.4.465

Olson, R. E. and J. Lai. 2004. *Apparatus Details for Triaxial Testing*. Taichung City, Taiwan: Chaoyang University of Technology.

Otani, J., T. Mukunoki, and Y. Obara. 2000. "Application of X-ray CT Method for Characterization of Failure in Soils." *Soils and Foundations* 40, no. 2 (April): 111–118. https://doi.org/10.3208/sandf.40.2_111

Ozbay, A. and A. F. Cabalar. 2016. "Effects of Triaxial Confining Pressure and Strain Rate on Stick-Slip Behavior of a Dry Granular Material." *Granular Matter* 18: 60. https://doi.org/10.1007/s10035-016-0664-7

Pan, B. 2009. "Reliability-Guided Digital Image Correlation for Image Deformation Measurement." *Applied Optics* 48, no. 8 (March): 1535–1542. https://doi.org/10.1364/AO.48.001535

Pedregosa, F., G. Varoquaux, A. Gramfort, V. Michel, B. Thirion, O. Grisel, M. Blondel, et al. 2011. "Scikit-Learn: Machine Learning in Python." *Journal of Machine Learning Research* 12: 2825–2830.

Peng, X. and J. G. Zornberg. 2019. "Evaluation of Soil-Geogrid Interaction Using Transparent Soil with Laser Illumination." *Geosynthetics International* 26, no. 2 (April): 206–221. https://doi.org/10.1680/jgein.19.00004

Rattez, H., Y. Shi, A. Sac-Morane, T. Klaeyle, B. Mielniczuk, and M. Veveakis. 2022. "Effect of Grain Size Distribution on the Shear Band Thickness Evolution in Sand." *Géotechnique* 72, no. 4 (April): 350–363. https://doi.org/10.1680/jgeot.20.P.120

Roscoe, K. H. 1970. "The Influence of Strains in Soil Mechanics." *Géotechnique* 20, no. 2 (June): 129–170. https://doi.org/10.1680/geot.1970.20.2.129

Saada, A. S., L. Liang, J. L. Figueroa, and C. T. Cope. 1999. "Bifurcation and Shear Band Propagation in Sands." *Géotechnique* 49, no. 3 (June): 367–385. https://doi.org/10.1680/geot.1999.49.3.367

Scrapelli, G. and D. M. Wood. 1982. "Experimental Observation of Shear Patterns in Direct Shear Tests." In *International Union of Theoretical and Applied Mechanics: Symposium on Deformation and Failure of Granular Materials Conference*. 473–483. Rotterdam, the Netherlands: A. A. Balkema.

Snyman, J. A. and D. N. Wilke. 2018. *Practical Mathematical Optimization: Basic Optimization Theory and Gradient-Based Algorithms*. 2nd ed. Cham, Switzerland: Springer International Publishing. https://doi.org/10.1007/978-3-319-77586-9

Stanier, S. A. *Modeling the Behaviour of Helical Screw Piles*. PhD Diss., University of Sheffield, 2011.

Stanier, S. A., J. A. Black, and C. C. Hird. 2012. "Enhancing Accuracy and Precision of Transparent Synthetic Soil Modelling." *International Journal of Physical Modelling in Geotechnics* 12, no. 4 (December): 162–175. https://doi.org/10.1680/ijpmg.12.00005

Stanier, S. A., J. Blaber, W. A. Take, and D. J. White. 2016. "Improved Image-Based Deformation Measurement for Geotechnical Applications." *Canadian Geotechnical Journal* 53, no. 5 (May): 727–739. https://doi.org/10.1139/cgj-2015-0253

Sutton, M. A., J.-J. Orteu, and H. W. Schreier. 2009. *Image Correlation for Shape, Motion and Deformation Measurements: Basic Concepts, Theory and Applications*. Boston, MA: Springer.

Tordesillas, A. and M. Muthuswamy. 2009. "On the Modeling of Confined Buckling of Force Chains." *Journal of the Mechanics and Physics of Solids* 57, no. 4 (April): 706–727. https://doi.org/10.1016/j.jmps.2009.01.005

van der Walt, S., J. L. Schönberger, J. Nunez-Iglesias, F. Boulogne, J. D. Warner, N. Yager, E. Gouillart, T. Yu, and the Scikit-Image Contributors. 2014. "Scikit-Image: Image Processing in Python." *PeerJ* 2: e453. https://doi.org/10.7717/peerj.453

Vardoulakis, I. 1980. "Shear Band Inclination and Shear Modulus of Sand in Biaxial Tests." *International Journal for Numerical and Analytical Methods in Geomechanics* 4, no. 2 (April/June): 103–119. https://doi.org/10.1002/nag.1610040202

Vardoulakis, I. and J. Sulem. 1995. *Bifurcation Analysis in Geomechanics*. 1st ed. Milton Park, UK: Taylor & Francis.

Vernese, F. J. and K. L. Lee. 1977. *Effect of Frictionless Caps and Bases in the Cyclic Triaxial Test, Report No. S-77-1*. Vicksburg, MS: US Army Engineer Waterways Experiment Station.

Weik, M. H. 2001. *Computer Science and Communications Dictionary*. Boston, MA: Springer.

White, D. J., W. A. Take, and M. D. Bolton. 2003. "Soil Deformation Measurement Using Particle Image Velocimetry (PIV) and Photogrammetry." *Géotechnique* 53, no. 7 (September): 619–631. https://doi.org/10.1680/geot.2003.53.7.619

Zhang, X., L. Li, G. Chen, and R. Lytton. 2015. "A Photogrammetry-Based Method to Measure Total and Local Volume Changes of Unsaturated Soils during Triaxial Testing." *Acta Geotechnica* 10, no. 1 (February): 55–82. https://doi.org/10.1007/s11440-014-0346-8

Zheng, J. and R. D. Hryciw. 2015. "Traditional Soil Particle Sphericity, Roundness and Surface Roughness by Computational Geometry." *Géotechnique* 65, no. 6 (June): 494–506. https://doi.org/10.1680/geot.14.P.192

Zuiderveld, K. 1994. "Contrast Limited Adaptive Histogram Equalization." In *Graphics Gems IV*, edited by P. S. Heckbert, 474–485. San Diego, CA: Academic Press Professional, Inc.